

Longqiu Li¹

Harbin Institute of Technology,
Harbin 150001, China;
University of California, San Diego,
La Jolla, CA 92093-0401
e-mail: longqiuli@gmail.com

Izhak Etsion

Fellow ASME
Technion-Israel Institute of Technology,
Haifa 32000, Israel

Andrey Ovcharenko

Frank E. Talke

Fellow ASME
University of California, San Diego,
La Jolla, CA 92093-0401

The Onset of Plastic Yielding in a Spherical Shell Compressed by a Rigid Flat

The onset of plastic yielding in a spherical shell loaded by a rigid flat is analyzed using finite element analysis. The effect of spherical shell geometry and material properties on the critical normal load, critical interference, and critical contact area, at the onset of plastic yielding, is investigated and the location where plastic yielding first occurs is determined. A universal dimensionless shell parameter, which controls the behavior of the spherical shell, is identified. An empirical relation is found for the load-interference behavior of the spherical shell prior to its plastic yielding. A limiting value of the dimensionless shell parameter is identified above which the shell behaves like a solid sphere. [DOI: 10.1115/1.4001994]

Keywords: spherical shell, yield inception, shell parameter

1 Introduction

The contact behavior of a deformable spherical shell of radius R , height H , and wall thickness t , that is loaded by a rigid flat with a load P and a corresponding interference ω (see Fig. 1(a)), is a problem of great interest in contact mechanics. Reissner [1] investigated the contact of a shallow spherical shell in the range of $H/R < 1/4$. His analysis provides expressions for direct stress resultants (N_{rr} and $N_{\theta\theta}$) and bending stress couples (M_{rr} and $M_{\theta\theta}$) in the meridian and circumferential direction, as shown in Fig. 1(b). It also provides a load-interference relationship for the spherical shell, which depends on the shell thickness ratio t/R and its material properties, Young's modulus E and Poisson's ratio ν . Naghdi [2] extended Reissner's solution [1] to include the effect of transverse shear strains, which was neglected in Ref. [1]. The shear strains are related to the transverse shear stress resultants V_{θ} and V_r , shown in Fig. 1(b), and to the normal stress (direct and bending) used in the stress-strain expressions for the shell. Essenberg [3] found that the effect of shear strain is essential for determining the distribution of surface tractions in a shell-flat interface. Updike and Kalnins [4,5] investigated the load-interference behavior of a hemispherical shell compressed by a rigid flat based on large deflection shell theory. It was shown in Ref. [4] that when the load increases, and the ratio ω/t becomes about 2, the initially flat contact region buckles into an axisymmetric dimple. The normal load and distribution of contact pressure between the shell and the flat before the buckling of the shell were determined.

Following Naghdi [2] and Essenberg [3], Schwartz et al. [6] theoretically solved the problem of a thin-walled shallow shell compressed by a rigid surface (for measuring intraocular pressure of the cornea of the eye). They showed that for an interference larger than $1/3$ of the shell thickness, the validity of the pressure distribution is questionable due to possible shell instability. Experimental investigations showed good correlation with theory for the load-interference relation. Kitching et al. [7], who were interested in collision of vehicles, ships, and submarines, investigated the load-interference behavior of a spherical shell as a function of the shell thickness ratio t/R . They used a multisegment direct numerical integration technique to solve the Reissner equation [1].

Good agreement was found between the theoretical and experimental studies. Gupta and Gupta [8,9] conducted theoretical and experimental studies on buckling of hemispherical shells of different thickness ratios, t/R , subjected to axial loads by a rigid flat. The experimental and theoretical results of the deformed shell shapes and their corresponding load-interference curves were in good agreement.

The shell-flat contact problem was also investigated by Pauchard et al. in Ref. [10] and by Pauchard and Rica in Ref. [11] (for the deformation of a "ping-pong" ball). Their experiments show a discontinuous transition between two different configurations: the first is characterized by a flat contact between the shell and the rigid flat, and the second by an inversion of curvature (buckling) leading to contact with the flat along a circular ridge. The condition for this transition is that the ratio ω/t becomes about 2, similar to the finding in Ref. [4]. In Refs. [10,11] the total energy, U , of an elastically deformed shell for the first configuration was presented as

$$U = \frac{C_0 E t^{5/2}}{4R} \omega^{3/2} + \frac{C_1 E t}{R} \omega^3 \quad (1)$$

where E is Young's modulus of the spherical shell, and C_0 and C_1 are the dimensionless parameters. The first term in Eq. (1) relates to the bending and stretching energies of a plate, and the second term relates to the compression of a portion of a sphere into a planer disk. The load-interference relationship for the first configuration mentioned above was obtained in Ref. [10] in the form

$$P = \frac{3C_0 E t^{5/2}}{8R} \omega^{1/2} + 3C_1 \frac{E t}{R} \omega^2 \quad (2)$$

All the above investigations [1–11] are limited to elastic deformations only where the stress-strain relationship remains linear even up to the onset of buckling. In many practical cases, however, plastic yielding of the compressed spherical shell can occur before buckling takes place [12,13]. Plastic buckling of a spherical shell compressed by a rigid flat was studied in several papers, e.g., Refs. [12–15], considering large interference in the range $\omega/t \geq 2$. It was shown that buckling depends on the spherical shell thickness ratio t/R and its material properties (Young's modulus E and Poisson's ratio ν).

Large plastic deformations should be preceded by onset of plastic yielding. Elastic-plastic contact and inception of yielding of a solid sphere loaded by a rigid flat can be considered a special case of the present problem when $t/R=1$. This situation was studied by

¹Corresponding author.

Contributed by the Applied Mechanics of ASME for publication in the JOURNAL OF APPLIED MECHANICS. Manuscript received October 13, 2009; final manuscript received May 22, 2010; accepted manuscript posted June 16, 2010; published online October 22, 2010. Assoc. Editor: Jian Cao.

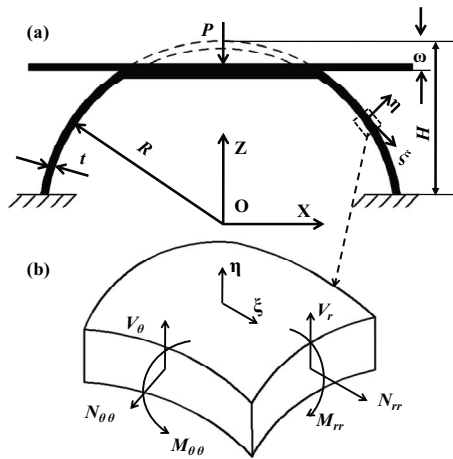


Fig. 1 Schematic sketch of a spherical shell compressed by a rigid flat (a), and direct stress resultants (N_{rr} , $N_{\theta\theta}$), bending stress couples (M_{rr} , $M_{\theta\theta}$) and shear stress resultants (V_θ , V_r) in meridian and circumferential direction for a typical shell segment (b)

several researchers e.g., Refs. [16–19]. It was found in these studies that a universal dimensionless expression can be obtained for the load-interference relation if the load and interference are normalized by their corresponding critical values at yield inception. However, no such investigations are available in the literature for the general case of $t/R < 1$. This paper is a first step in an attempt to fill this gap. In particular, the main goal of the present work is to study the yield inception of a spherical shell as a function of shell geometry and material properties, and compare the results with the published model of a solid sphere contacting a rigid flat [19]. It is hoped that such results will enable in future work to obtain universal dimensionless expressions for elastic-plastic loading of spherical shells in a similar way to the case of solid spheres. A possible application is, for example, the contact deformation of the dimple/gimbal interface in a hard disk drive suspension [20].

2 Finite Element Model of the Spherical Shell

Figure 2 presents the axisymmetric 2D model that was analyzed using implicit integration method with the commercially available finite element software ANSYS (version 11.0). Two meshing approaches were used depending on the ratio t/R . For small values of t/R , i.e., for $t/R \leq 0.05$, the shell was divided into two different mesh density zones (see Fig. 2(a)). Zone I, within a distance of $0.06R$ from the spherical shell tip, had a very fine mesh to accurately capture the high stress gradients in this zone. Zone II, outside the $0.06R$ region, had a gradually coarser mesh with increasing distance from the spherical shell tip. For $t/R > 0.05$, the shell was divided into four different mesh density zones (see Fig. 2(b)), where zones I, II, and III were within $0.01R$, $0.025R$, and $0.05R$, respectively, from the sphere summit, and zone IV was outside the $0.05R$. Zone I had the finest mesh and the other regions had gradually coarser meshes. The flat was modeled as a rectangle having the dimensions $0.1R \times 0.05R$ in the X and Z directions, respectively. A finer mesh was used close to the contact zone, as shown in the insets of Figs. 2(a) and 2(b). An eight-node axisymmetric quadrilateral element (PLANE183) was used for the bulk of the spherical shell and flat. A three-node contact element (Conta172) and target element (Targe169) were used on the contacting surfaces of the spherical shell and rigid flat, respectively. The entire mesh consisted of 14,210–28,763 elements, and 38,790–76,978 nodes depending on the shell thickness ratio, t/R .

The following boundary conditions were imposed (see Fig. 3):

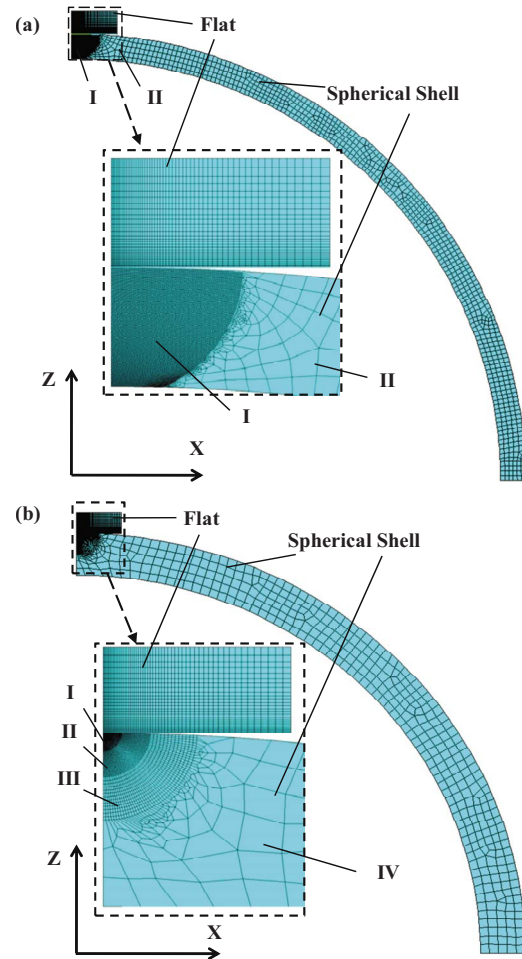


Fig. 2 Mesh of the finite element model for a small thickness ratio $t/R \leq 0.05$ (a) and for a larger thickness ratio $t/R > 0.05$ (b). Zones I, II, III, and IV represent different mesh densities.

- The nodes on the axis of symmetry Z of the flat and spherical shell were restricted in the X direction.
- The nodes at the base of the hemispherical shell were re-

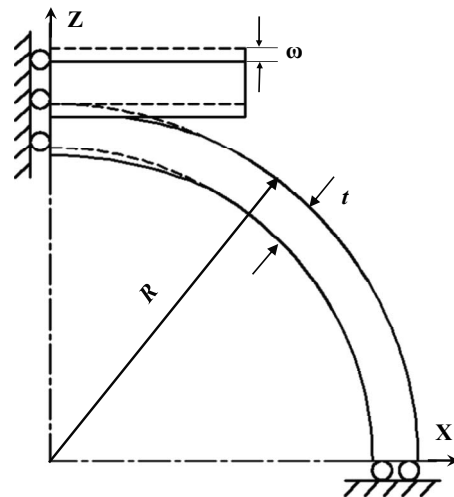


Fig. 3 Schematic of the model of spherical shell contacting a rigid flat and its boundary conditions

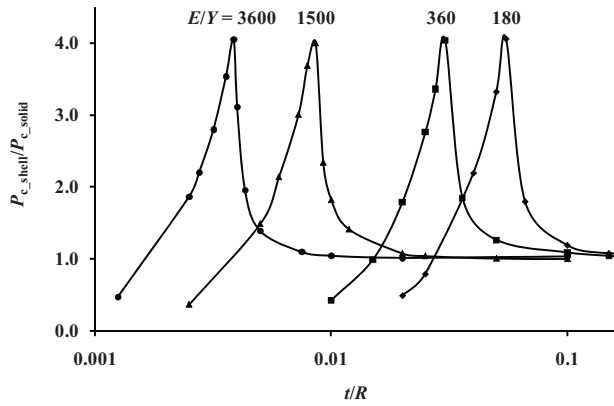


Fig. 4 The critical load ratio, P_{c_shell}/P_{c_solid} , versus the thickness ratio, t/R , at different values of E/Y

- stricted in the Z direction only. Fixing these nodes had a negligible effect (less than 1%) on the results.
- The nodes at the top of the flat were coupled in order to maintain pure translations of the flat, without tilt, i.e., their displacement vectors were forced to be equal in the Z direction.
 - Frictionless contact condition was assumed between the shell and flat.

Displacement control of the rigid flat was used for loading the shell. Hence, the interference ω of the shell was an input for the numerical simulations and the normal load P was obtained as an output for any given interference. The following input values were used for the shell: spherical shell radii $R=200, 500, 1000 \mu\text{m}$; shell thickness ratio $0.00125 \leq t/R \leq 1$; Young's modulus $E_{shell}=180 \text{ GPa}$; yield strength $Y=50 \text{ MPa}, 120 \text{ MPa}, 500 \text{ MPa},$ and 1000 MPa ; Poisson's ratio $\nu=0.31$. The material behavior for the spherical shell was assumed to be elastic-plastic with linear isotropic hardening and a tangent modulus of 2% of Young's modulus. To simulate a rigid flat, Young's modulus of the flat was chosen to be $E_{flat}=1000E_{shell}$. The von Mises yield criterion was used to detect the onset of plastic deformation.

To verify the validity of the finite element model, the results for shell thickness ratio $t/R=1$ were compared with the Hertz solution [21]. The error of the numerically obtained contact load was less than 3%. Proper convergence of the numerical solution was tested by refining the mesh size (increasing the number of elements) by at least one order of magnitude. The CPU times for each case varied from about 10 min to 30 min, on a 2.4 GHz Quad CPU with 4 Gbyte memory HP workstation.

3 Results and Discussion

The critical normal load P_{c_shell} at yield inception of the spherical shell, normalized by that for a solid sphere P_{c_solid} , is presented in Fig. 4 as a function of t/R for different values of E/Y . The critical load P_{c_solid} of a solid sphere is [19]

$$P_{c_solid} = \frac{\pi^3}{6} C_v^3 Y \left(R(1-\nu^2) \frac{Y}{E} \right)^2 \quad (3)$$

where $C_v=1.234+1.256\nu$.

As can be seen from Fig. 4, the critical load ratio P_{c_shell}/P_{c_solid} , which is plotted as a function of t/R on a semilog scale, has a very similar behavior for all values of E/Y investigated. In all cases shown in Fig. 4, a peak value of $P_{c_shell}/P_{c_solid}=4$ is obtained at a certain value of $t/R=(t/R)_p$, which depends on E/Y and decreases as E/Y becomes larger. The critical load ratio P_{c_shell}/P_{c_solid} changes sharply in a narrow transition zone around its peak value and approaches the value of 1

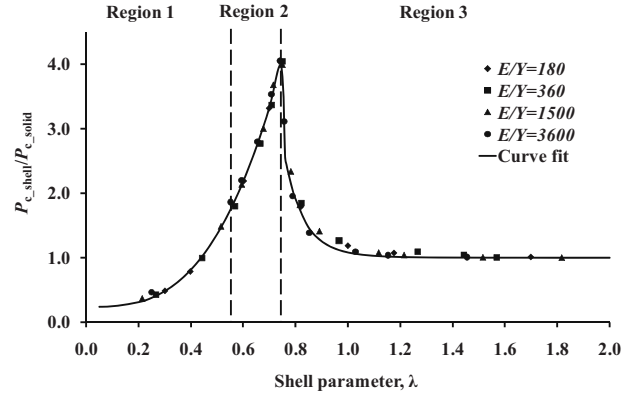


Fig. 5 The critical load ratio, P_{c_shell}/P_{c_solid} , versus the shell parameter λ

when t/R exceeds its corresponding $(t/R)_p$. The relation between $(t/R)_p$ and E/Y can be obtained by curve fitting the results using the form

$$\log\left(\frac{t}{R}\right)_p = 0.75 - 0.886 \log\left(\frac{E}{Y}\right) \quad (4)$$

Equation (4) can be rearranged in the form

$$\log\left(\left(\frac{t}{R}\right)_p \left(\frac{E}{Y}\right)^{0.886}\right) = 0.75 = \lambda_p \quad (5)$$

where λ is the new dimensionless "shell parameter" given by

$$\lambda = \log\left(\frac{t}{R} \left(\frac{E}{Y}\right)^{0.886}\right) \quad (6)$$

Plotting the critical load ratio versus λ consolidates the various E/Y cases shown in Fig. 4 into a single universal curve. The value $\lambda_p=0.75$ (see Eq. (5)) marks the common value corresponding to the maximum critical load ratio $P_{c_shell}/P_{c_solid}=4$, as shown in Fig. 5. Hence, the critical load ratio can be described as a unique function of the universal shell parameter λ in the form

$$\frac{P_{c_shell}}{P_{c_solid}} = f_1(\lambda) = a_1 \lambda^{b_1} + c_1 \quad (7)$$

Three regions of the shell parameter λ values are marked in Fig. 5. As will be discussed later, these regions correspond to three different typical locations of the yield inception.

Similar to the case of the critical load ratio, the shell parameter λ given in Eq. (6) can be used to describe the behavior of the critical interference ratio $\omega_{c_shell}/\omega_{c_solid}$, where ω_{c_shell} and ω_{c_solid} denote the critical interference at yield inception of a spherical shell and a solid sphere, respectively. The critical interference ω_{c_solid} of a solid sphere is given by [19]

$$\omega_{c_solid} = \frac{\pi}{2} C_v R (1-\nu^2) \left(\frac{Y}{E}\right)^2 \quad (8)$$

Figure 6 presents the critical interference ratio $\omega_{c_shell}/\omega_{c_solid}$ as a function of the shell parameter λ for different values of E/Y . As can be seen from Fig. 6, the critical interference ratio increases slightly with increasing λ and reaches a peak value, which depends on E/Y , at the same $\lambda_p=0.75$ that marks the maximum critical load ratio (see Fig. 5). Thereafter, the critical interference ratio decreases sharply and approaches unity. This trend is similar to that of the critical load ratio shown in Fig. 5.

The different curves shown in Fig. 6 can be consolidated into one universal curve, as shown in Fig. 7, by using the transformation

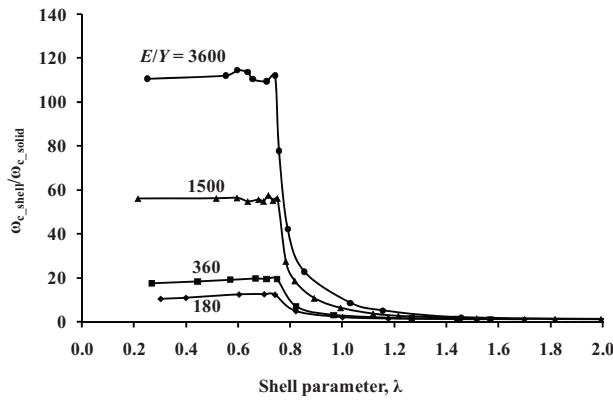


Fig. 6 The critical interference ratio, $\omega_{c_shell}/\omega_{c_solid}$, versus the shell parameter λ at different E/Y values

$$\log_{\alpha} \left(\frac{\omega_{c_shell}}{\omega_{c_solid}} \right) = f_2(\lambda) \quad (9)$$

where α is a function of E/Y . Using least squares curve fitting of the numerical results in Fig. 7 one can express α as

$$\alpha = 0.23 \left(\frac{E}{Y} \right)^{0.75} \quad (10)$$

and Eq. (9) can be expressed in the form

$$\frac{\log \left(\frac{\omega_{c_shell}}{\omega_{c_solid}} \right)}{\log \alpha} = f_2(\lambda) = a_2 \lambda^{b_2} + c_2 \quad (11)$$

Note that for $\lambda \leq 0.75$ the function $f_2(\lambda)$ in Fig. 7 is close to 1, i.e., the ratio $\omega_{c_shell}/\omega_{c_solid}$ in this range of λ values depends solely on E/Y , regardless of the thickness ratio t/R .

The critical contact area ratio A_{c_shell}/A_{c_solid} as a function of λ shows very similar behavior to that of the critical load ratio (see

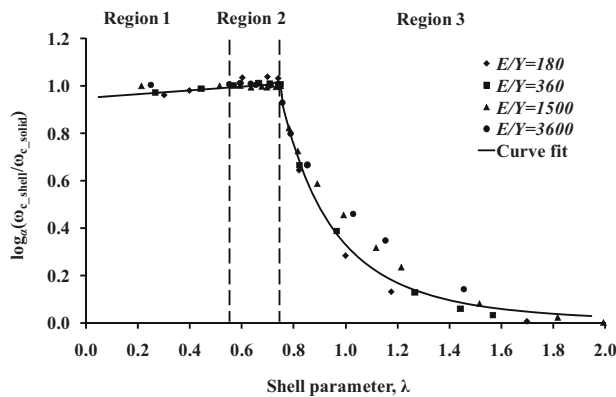


Fig. 7 The dimensionless expression $\log_{\alpha}(\omega_{c_shell}/\omega_{c_solid})$, versus the shell parameter λ

Table 1 Values of the constants used in Eqs. (7), (11), and (12)

i	$\lambda \leq 0.75$			$\lambda > 0.75$		
	1	2	3	1	2	3
a_i	9.03	0.08	4.49	0.082	0.33	0.25
b_i	2.97	1.00	2.15	-10.72	-3.68	-4.94
c_i	0.24	0.95	0.58	1.00	0.00	1.00

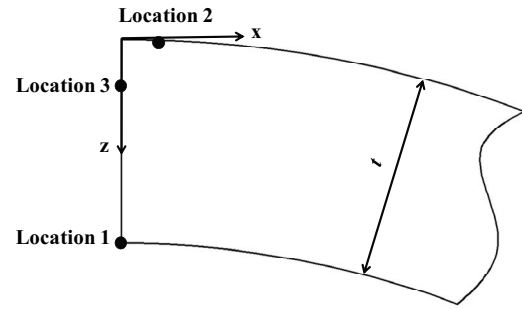


Fig. 8 A schematic description of the three typical locations of yield inception within the spherical shell, corresponding to the three regions, respectively, of the shell parameter λ values shown in Figs. 5 and 7

Fig. 5) but with a peak value of 3 instead of 4 at $\lambda = \lambda_p = 0.75$. Curve fitting the numerical results for the critical contact area ratio provided the following empirical relation:

$$\frac{A_{c_shell}}{A_{c_solid}} = f_3(\lambda) = a_3 \lambda^{b_3} + c_3 \quad (12)$$

The constants a_i , b_i , and c_i ($i=1, 2, 3$) of Eqs. (7), (11), and (12) were found from numerical simulations for various values of the shell parameter λ in the range of $0.00125 \leq t/R \leq 1$ and E/Y values from 180 to 3600, and are summarized in Table 1.

The effect of the shell height H (see Fig. 1) on the critical load and critical interference ratio was investigated over the range of shell height ratio $0.2 \leq H/R \leq 1$. In this range of H/R values, the deviation from the results obtained by Eqs. (7), (11), and (12) was less than 3%.

Yield inception can occur in three different typical locations within the spherical shell. These locations, which are shown schematically as location 1, location 2, and location 3 in Fig. 8, correspond to the three regions of λ values marked in Figs. 5 and 7. When $\lambda < 0.55$ ("region 1" in Fig. 5), the first plastic deformation occurs at a single point located on the Z axis and on the inner surface of the spherical shell ("location 1" in Fig. 8). In this region, the critical load ratio P_{c_shell}/P_{c_solid} and the critical interference ratio $\omega_{c_shell}/\omega_{c_solid}$ increase with increasing λ . When $0.55 \leq \lambda \leq 0.75$, which is marked as "region 2" in Fig. 5, the first plastic deformation occurs on a circle close to the edge of the contact area and just below the contact surface ("location 2" in Fig. 8). In this narrow region of λ values, both P_{c_shell}/P_{c_solid} and $\omega_{c_shell}/\omega_{c_solid}$ continue to increase with increasing λ , reaching their peak values at $\lambda_p = 0.75$. When $\lambda > 0.75$ ("region 3" in Fig. 5), the yield inception occurs again at a single point located on the axis of symmetry, Z, slightly below the contact surface ("location 3" in Fig. 8). In this region, the critical load and critical interference ratios decrease sharply with increasing λ and become unity at $\lambda \geq 2$ where the spherical shell behaves similar to a solid sphere.

To understand the effect of λ on the three different yield inception locations presented in Fig. 8, the stress distribution within the shell, for the critical interference, ω_{c_shell} , was analyzed for the axis of symmetry and for a radial line located slightly below the

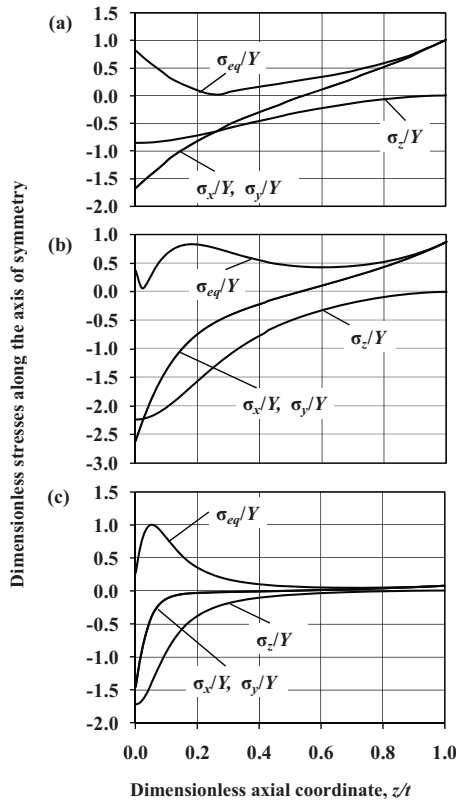


Fig. 9 Dimensionless stresses versus the dimensionless coordinate z/t along the axis of symmetry for the critical interference, ω_{c_shell} , and three typical values of the shell parameter: (a) $\lambda=0.2$, (b) $\lambda=0.7$, and (c) $\lambda=1.0$

contact surface at a distance $z/t=0.05$ (note the origin of the coordinate system $x-z$ in Fig. 8). Three typical values of the shell parameter λ were selected, namely, 0.2, 0.7, and 1.0, for the analysis. These λ values correspond to region 1, region 2, and region 3, respectively, which are shown in Figs. 5 and 7.

The von Mises yield criterion can be expressed as

$$Y = \sigma_{eq} = \left\{ \frac{1}{2} [(\sigma_1 - \sigma_2)^2 + (\sigma_2 - \sigma_3)^2 + (\sigma_1 - \sigma_3)^2] \right\}^{1/2} \quad (13)$$

where σ_1 , σ_2 , and σ_3 are the principal stresses, σ_{eq} is the equivalent von Mises stress, and Y is the yield strength of the spherical shell material.

Along the axis of symmetry $\tau_{xy}=\tau_{yz}=\tau_{xz}=0$ and the principal stresses are σ_x , σ_y and σ_z . Figure 9 shows the normalized principal stresses and the equivalent von Mises stress obtained by

$$\sigma_{eq} = \left\{ \frac{1}{2} [(\sigma_x - \sigma_y)^2 + (\sigma_y - \sigma_z)^2 + (\sigma_x - \sigma_z)^2] \right\}^{1/2} \quad (14)$$

versus the dimensionless coordinate z/t along the axis of symmetry, for the three different values of the shell parameter λ . As can be seen from Fig. 9, σ_x has the same values as σ_y due to the axisymmetric contact problem, and σ_z vanishes on the free inner surface of the shell at $z/t=1$, as would be expected.

In regions 1 and 2 (see Figs. 9(a) and 9(b)), when the shell parameter $\lambda \leq 0.75$ and hence, the thickness ratio t/R is small (see Eq. (6)), the normal stresses σ_x and σ_y have both negative and positive values. This is due to possible bending caused by the normal loading of the thin spherical shell. In particular, there is tension (positive stress values) close to the inner shell surface ($z/t=1$) and compression (negative values) close to the outer shell surface ($z/t=0$). The neutral surface, where σ_x and σ_y are zero, is located at about $z/t=0.5$. In region 1, the normalized equivalent

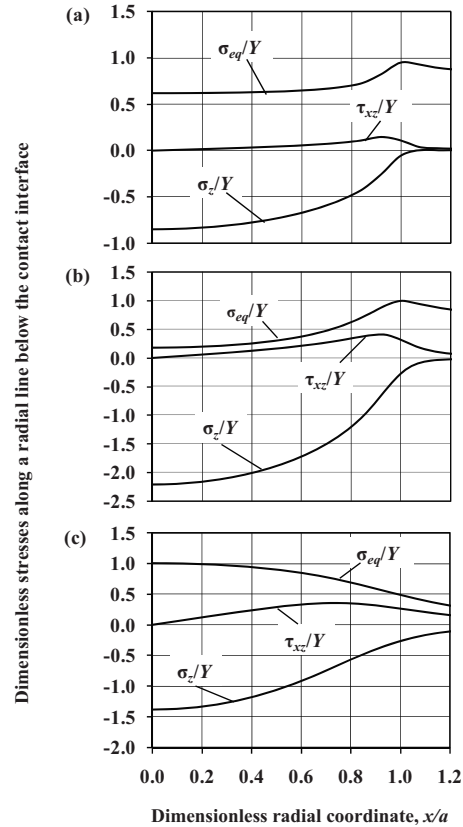


Fig. 10 Dimensionless stresses along the dimensionless radial coordinate x/a at $z/t=0.05$ for the critical interference, ω_{c_shell} , and three typical values of the shell parameter: (a) $\lambda=0.2$, (b) $\lambda=0.7$, and (c) $\lambda=1.0$

von Mises stress, σ_{eq}/Y , equals unity on the inner surface ($z/t=1$) where the yield inception in region 1 is located (see Fig. 8). In region 2, $\sigma_{eq}/Y < 1$ for the entire range of z/t , as shown in Fig. 9(b); hence, in this transition region plastic yielding does not occur on the axis of symmetry. In region 3 (Fig. 9(c)) when the shell parameter $\lambda > 0.75$, and the thickness ratio t/R is large, the maximum normalized von Mises stress ($\sigma_{eq}/Y=1$) is located around $z/t=0.05$. This is similar to the location obtained from the Hertz solution for a solid sphere. Also in region 3 at $z/t > 0.6$, far away from the contact zone, all stresses diminish to very small values.

In Fig. 10, the dimensionless normal stress σ_z/Y , shear stress τ_{xz}/Y , and equivalent von Mises stress σ_{eq}/Y , at $z/t=0.05$ below the contact interface, are presented versus the dimensionless radial coordinate x/a (where a is the contact radius) for the same three values of the shell parameter λ shown in Fig. 9. As can be seen from the figure, σ_z follows the contact pressure, which is close to zero at the contact area edge when $x/a=1$. In regions 1 and 2 (Figs. 10(a) and 10(b), respectively), the highest shear stress, τ_{xz} , is near the edge of the contact area, resulting in maximum von Mises stress at this location. In region 1, the maximum von Mises stress σ_{eq}/Y at the edge of the contact area is slightly below 1. In region 2 (Fig. 10(b)) $\sigma_{eq}/Y=1$ around that edge and hence, yield inception occurs there as shown by location 2 in Fig. 8. In region 3 (Fig. 10(c)), the behavior of the stresses is similar to that in a solid sphere.

Figure 11 presents the contour plot of the through-thickness von Mises stresses for the three different values of the shell parameter λ presented in Figs. 9 and 10. The results were obtained for $E/Y=1500$ and three different t/R values from 0.0025 to 0.015. These plots clearly demonstrate and explain the different locations of yield inception discussed above.

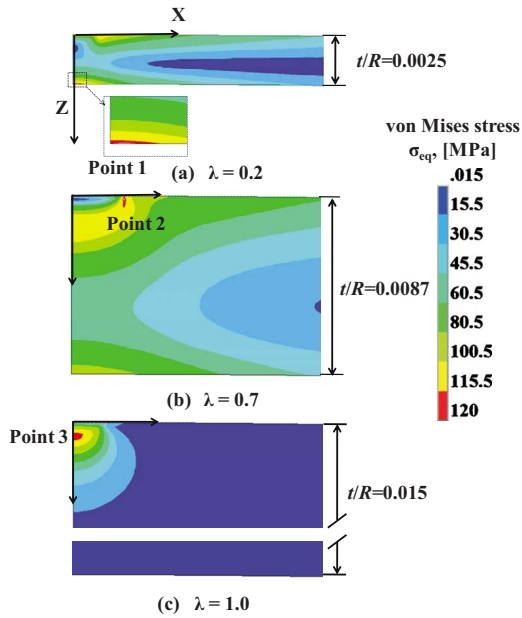


Fig. 11 Contour plot of the through-thickness von Mises stresses for the critical interference, ω_{c_shell} , and three typical values of the shell parameter: (a) $\lambda=0.2$, (b) $\lambda=0.7$, and (c) $\lambda=1.0$

The results shown in Figs. 9–11 as well as those in Figs. 5 and 7 imply the existence of two different mechanisms for the yield inception, depending on the shell parameter λ . For $\lambda \leq \lambda_p$ (regions 1 and 2), the first yield occurs due to bending of the spherical shell. When $\lambda > \lambda_p$ (region 3), the first yielding occurs due to compression of the relatively thicker shell, which in this region acts similar to a solid sphere. In this latter case, yield inception occurs at a single point slightly below the contact interface. When λ approaches λ_p yield inception takes place on a much larger volume around the edge of the contact area. The fact that more material yielded in region 2 may explain the higher critical normal load in this region compared with that in region 3 (see Fig. 5).

Finally, it is of interest to determine the relationship between the dimensionless normal load $P^* = P/P_{c_shell}$ and the dimensionless interference $\omega^* = \omega/\omega_{c_shell}$, over the entire range of λ values. For large λ values, where the spherical shell behaves like a solid sphere (see Figs. 5 and 7), the Hertz solution is expected. Hence,

$$P^* = (\omega^*)^{1.5} \quad (15)$$

For small interference values, $\omega/t < 2$, which may correspond to medium λ values, it was demonstrated in Ref. [10] that the normal load P is proportional to $\omega^{1.2}$. Hence, in this range the following relation is expected:

$$P^* = (\omega^*)^{1.2} \quad (16)$$

From Eqs. (15) and (16), it seems that a general relationship in the form

$$P^* = (\omega^*)^\beta \quad (17)$$

may cover the entire range of λ values. Indeed, from a very large number of numerical simulations, it became possible to find the empirical dependence of β on λ (see Fig. 12). A best fit of the numerical results shown in Fig. 12 gives the following relation:

$$\beta = \begin{cases} 1.0, & \lambda \leq 0.75 \\ 0.42\lambda + 0.68, & 0.75 < \lambda < 2 \\ 1.5, & \lambda \geq 2 \end{cases} \quad (18)$$

Figure 13 presents the results of Eqs. (17) and (18) in comparison with the results of the Hertz solution (Eq. (15)) and those

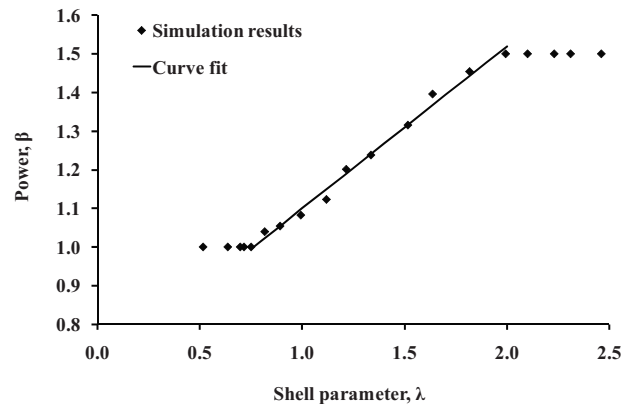


Fig. 12 The power β used in Eq. (17) as a function of the shell parameter λ

obtained in Ref. [10]. (Eq. (16)). The latter correspond, according to Eq. (18), to a shell parameter value of $\lambda=1.24$, which is in region 3 where the thickness t may be large enough to fulfill the condition of Ref. [10], namely, $\omega_{c_shell}/t < 2$, but not too large to exhibit a behavior of a solid sphere (see Fig. 7).

Figure 13 and Eq. (18), like Figs. 5 and 7, demonstrate the different behaviors of the spherical shell depending on the shell parameter λ . For $\lambda \leq \lambda_p$ (regions 1 and 2), the relationship between the dimensionless normal load P^* and the dimensionless interference ω^* is linear, and the spherical shell behaves like a linear spring. In this case the dimensionless elastic energy stored by the spherical shell, which is the area under the dimensionless load-interference curve in Fig. 13, is the largest of all the other cases. The total energy in this case consists of the bending energy, stretching energy, and compression of a portion of a sphere energy [10,11]. When $\lambda > \lambda_p$ (region 3), the dimensionless elastic energy stored by the spherical shell decreases with increasing λ and at $\lambda \geq 2.0$, it becomes that of a solid sphere. This can also explain the higher critical load and critical interference that are required for the yielding of the spherical shell at $\lambda=\lambda_p$ in comparison to that for the solid sphere.

It should be noted here that the discontinuous transition observed in Figs. 5 and 7 at $\lambda=\lambda_p$ is very different from the discontinuous transition described, for example, in Ref. [11]. In the latter case, the transition is associated with a change from a planar contact between the shell and the flat to a circular ridge contact due to the buckling of the elastic shell. This transition occurs when the ratio $\omega/t \approx 2$. In the present study, the transition is associated with a change in the location of yield inception from an annulus slightly below the edge of the contact area in region 2 to

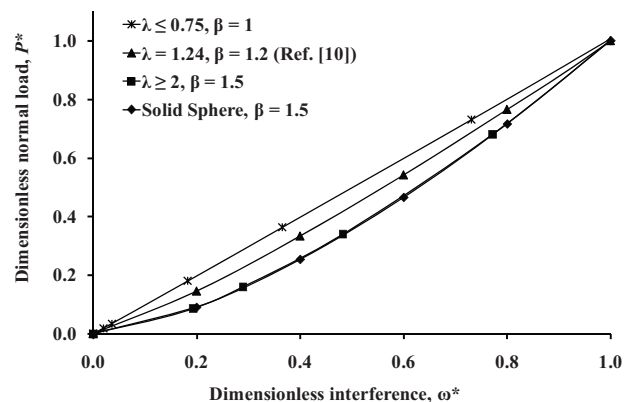


Fig. 13 The dimensionless normal load P^* , as a function of the dimensionless interference ω^* , prior to yield inception

a point on the axis of symmetry in region 3. The ratio ω/t corresponding to this transition in the location of yield inception is less than 0.04 for all λ values covered in the present analysis. Moreover, no loss of contact between the shell and the flat was found even for the smallest thickness ratio $t/R=0.00125$. Hence, over the range of λ values investigated in this paper, yield inception seems to occur much earlier than buckling.

4 Conclusion

A 2D axisymmetric model for the onset of plastic yield in a spherical shell loaded by a rigid flat was developed. A universal shell parameter λ , which controls the behavior of the spherical shell, was identified. Two main regions of the shell parameter λ , with a narrow transition region between them, were identified corresponding to three different locations of the yield inception. The critical load ratio P_{c_shell}/P_{c_solid} can be expressed as a unique function of the shell parameter λ regardless of the dimensional shell geometry and its material properties. The critical interference ratio $\omega_{c_shell}/\omega_{c_solid}$ is a function of both λ and E/Y . At the end of the transition region, when $\lambda=\lambda_p=0.75$ the critical load and interference ratios attain their peak values. For $\lambda \geq 2.0$ the spherical shell behaves like a solid sphere.

An empirical relationship in the form $P^*=(\omega^*)^\beta$ was found for the load-interference behavior of the spherical shell prior to its plastic yielding. The value, $\lambda_p=0.75$, also marks a change in that behavior. For $\lambda \leq \lambda_p$, the elastic stiffness of the spherical shell is linear, and the dimensionless elastic energy stored in it is maximum. When $\lambda > \lambda_p$, the elastic stiffness becomes nonlinear, the dimensionless elastic energy stored in the deformed shell decreases with increasing λ and at $\lambda \geq 2.0$, it becomes that of a solid sphere. In the range of λ values above 0.2 yield inception always occurs before any buckling even when the shell thickness ratio is as small as 0.00125.

Acknowledgment

We gratefully acknowledge partial support of this work by the NHK International Corp. L.L. also thanks the China Scholarship Council (CSC), and Professor G. Zhang from Harbin Institute of Technology, for supporting his Ph.D. study at UCSD.

Nomenclature

A_{c_solid}	= critical contact area of a solid sphere
A_{c_shell}	= critical contact area of a spherical shell
a	= radius of the contact area
E	= Young's modulus
H	= height of the spherical shell
P	= normal load
P_{c_solid}	= critical normal load of a solid sphere
P_{c_shell}	= critical normal load of a spherical shell
P^*	= dimensionless normal load, P/P_{c_shell}
R	= radius of the spherical shell
t	= thickness of the spherical shell
Y	= yield strength
λ	= shell parameter, $\log[(t/R)(E/Y)^{0.886}]$

λ_p	= shell parameter corresponding to maximum critical parameters ratio
ω	= interference
ω_{c_solid}	= critical interference of a solid sphere
ω_{c_shell}	= critical interference of a spherical shell
ω^*	= dimensionless interference, ω/ω_{c_shell}
ν	= Poisson's ratio
$\sigma_1, \sigma_2, \sigma_3$	= principal stresses
σ_{eq}	= equivalent von Mises stress
$\sigma_x, \sigma_y, \sigma_z$	= normal stresses
$\tau_{xy}, \tau_{yz}, \tau_{xz}$	= shear stresses

References

- [1] Reissner, E., 1947, "Stresses and Small Displacements of Shallow Spherical Shells," *J. Math. Phys.*, **25**(3), pp. 279–300.
- [2] Naghdi, P., 1956, "Note on the Equation for Shallow Spherical Shells," *Q. Appl. Math.*, **14**, pp. 369–380.
- [3] Essenberg, F., 1962, "On Surface Constraint in Plate Problems," *Trans. ASME, J. Appl. Mech.*, **29**, pp. 340–344.
- [4] Updike, D. P., and Kalnins, A., 1970, "Axisymmetric Behavior of an Elastic Spherical Shell Compressed Between Rigid Plates," *Trans. ASME, J. Appl. Mech.*, **37**, pp. 635–640.
- [5] Updike, D. P., and Kalnins, A., 1972, "Contact Pressure Between an Elastic Spherical Shell and a Rigid Flat," *Trans. ASME, J. Appl. Mech.*, **39**, pp. 1110–1114.
- [6] Schwartz, N. J., Mackay, R. S., and Sackman, J. L., 1966, "A Theoretical and Experimental Study of the Mechanical Behavior of the Cornea With Application to the Measurement of Intraocular Pressure," *Bull. Math. Biophys.*, **28**(4), pp. 585–643.
- [7] Kitching, R., Houlston, R., and Johnson, W., 1975, "A Theoretical and Experimental Study of Hemispherical Shells Subjected to Axial Loads Between Flat Plates," *Int. J. Mech. Sci.*, **17**, pp. 693–703.
- [8] Gupta, P. K., and Gupta, N. K., 2006, "An Experimental and Computational Study of the Crushing of Metallic Hemispherical Shells Between Two Rigid Flat Plates," *J. Strain Anal. Eng. Des.*, **41**(6), pp. 453–466.
- [9] Gupta, P. K., and Gupta, N. K., 2009, "A Study of Axial Compression of Metallic Hemispherical Domes," *J. Mater. Process. Technol.*, **209**, pp. 2175–2179.
- [10] Pauchard, L., Pomeau, Y., and Rica, S., 1997, "Déformation des Coques Élastiques," *Acad. Sci., Paris, C. R.*, **324**, pp. 411–418.
- [11] Pauchard, L., and Rica, S., 1998, "Contact and Compression of Elastic Spherical Shell: The Physics of a 'Ping Pong' Ball," *Philos. Mag. B*, **78**, pp. 225–233.
- [12] Updike, D. P., and Kalnins, A., 1972, "Axisymmetric Post-Buckling and Non-Symmetric Buckling of a Spherical Shell Compressed Between Rigid Plates," *Trans. ASME, J. Appl. Mech.*, **39**, pp. 172–178.
- [13] Hutchinson, J. W., 1972, "On the Post-Buckling Behavior of Imperfection-Sensitive Structures in the Plastic Range," *Trans. ASME, J. Appl. Mech.*, **39**, pp. 155–162.
- [14] Updike, D. P., 1972, "On the Large Deformation of a Rigid-Plastic Spherical Shell Compressed by a Rigid Plate," *Int. J. Mech. Sci.*, **94**(3), pp. 949–955.
- [15] Nowinka, J., and Lukasiewicz, S., 1994, "Hemisphere Compressed by Rigid Plates," *Int. J. Non-Linear Mech.*, **29**(1), pp. 23–29.
- [16] Chang, W. R., Etsion, I., and Bogy, D. B., 1987, "An Elastic-Plastic Model for the Contact of Rough Surfaces," *Trans. ASME, J. Tribol.*, **109**, pp. 257–263.
- [17] Kogut, L., and Etsion, I., 2002, "Elastic-Plastic Contact Analysis of a Sphere and a Rigid Flat," *Trans. ASME, J. Appl. Mech.*, **69**, pp. 657–662.
- [18] Jackson, R. L., and Green, I., 2005, "A Finite Element Study of Elasto-Plastic Hemispherical Contact Against a Rigid Flat," *Trans. ASME, J. Tribol.*, **127**, pp. 343–354.
- [19] Brizmer, V., Kligerman, Y., and Etsion, I., 2006, "The Effect of Contact Conditions and Material Properties on the Elasticity Terminus of a Spherical Contact," *Int. J. Solids Struct.*, **43**, pp. 5736–5749.
- [20] Raeymaekers, B., Helm, S., Brunner, R., Fanslau, E. B., and Talke, F. E., 2010, "Investigation of Fretting Wear at the Dimple/Gimbal Interface in a Hard Disk Drive Suspension," *Wear*, **268**, pp. 1347–1353.
- [21] Johnson, K. L., 1985, *Contact Mechanics*, Cambridge University Press, Cambridge, UK.